Unified method for measuring entropy differences between coexisting surface phases using low energy electron microscopy

M. Ivanov ●,[1] D. Gomez ●,[1] K. Hannikainen,[1] Y. R. Niu,[1,2] and J. Pereiro ●[1,*]

[1]*School of Physics and Astronomy, Cardiff University, Queen's Buildings, The Parade, Cardiff CF24 3AA, United Kingdom*
[2]*MAX IV Laboratory, Fotongatan 2, 22484 Lund, Sweden*

We demonstrate the ability of low energy electron microscopy (LEEM) to extract fundamental information in surface phase transitions during *in situ* observations of complex semiconductor surfaces. We utilize established LEEM techniques and develop a methodology that enables us to calculate the surface entropy difference using only LEEM measurements without the need for external characterization. We demonstrate the effectiveness of the unified method by monitoring the phase coexistence during the first-order transition between the $c(8 \times 2)$ and (6×6) phases on the surface of GaAs(001) at a range of temperatures relevant for epitaxy. The coexistence behavior with temperature and the fluctuations of phase boundaries are measured and analyzed to obtain the entropy difference and stress difference between the phases. The calculated values show that the entropy difference is not large enough to stabilize the (6×6) phase with respect to the $c(8 \times 2)$ by itself, suggesting that the elastic relaxation during the coexistence between the two phases is necessary to stabilize the (6×6) phase.

I. INTRODUCTION

Entropy is a key thermodynamic property of the semiconductor surface that governs much of the surface phase behavior. Its contribution to surface energetics can be a valuable consideration in theoretical surface models, but measuring entropy differences between phases experimentally is elusive and the parameter is usually neglected. In this work, we show that in the context of a first-order phase transition, this can be achieved through three sets of measurements within a single experiment using low energy electron microscopy (LEEM). LEEM microscopy has been established as one of the most effective methods for the detection of phase coexistence [1,2] and its ability to observe surface dynamics in real time with great precision allows the measurements of the phase coverage and boundary fluctuations, which can then be analyzed with the methods reviewed by Hannon and Tromp [3].

The understanding and control of the GaAs(001) semiconductor surface structure is a crucial factor in maintaining the high quality of epitaxial growth for the high-precision fabrication of heterostructures for optoelectronic devices [4–10]. As a result, the structure, defined by its surface phases, has been extensively studied and considerable understanding of the behavior and underlying processes has been reached [11–13]. A significant part of that behavior, especially during some phase transitions, is the possibility of having multiple surface phases simultaneously. This phase coexistence phenomenon can be successfully accounted for by the energetics of long-range elastic and electrostatic interactions [14–18] and its stability is largely governed by two fundamental parameters: the stress difference and the entropy difference between the two phases [19]. The elastic and electrostatic interactions, which are dependent on the surface phase coverage, give access to the entropy difference. The stress difference manifests itself through the stiffness of the boundaries between the two coexisting phases and so it is found by closely monitoring the boundary fluctuations [20,21].

We bring together methods in LEEM imaging and analysis and demonstrate their ability to obtain fundamental surface parameters of a compound semiconductor independently and without the need for external characterization. We develop a modular computational algorithm to automate the analysis process, making the method easily applicable to most semiconductor and metallic surfaces [22].

Our experimental observations focus on the stable phase coexistence between the (6×6) and the $c(8 \times 2)$ as we aim to settle the ongoing debate about the stability of the (6×6) phase. Multiple (6×6) geometries have been determined through theoretical calculations, but were shown to not be stable [11,23,24]. Details on these calculations are given in the Appendix 1. Despite the predicted instability, multiple surface structures and compositions of the phase were experimentally observed using scanning tunneling microscopy measurements [24]. LEEM microscopy was recently used to observe that the (6×6) phase manifests itself on the GaAs(001) surface through three separate regimes, depending on the experimental conditions. In its low-temperature regime, it can indeed be stable within a very narrow window and cover most of the surface area, as observed through control over the chemical potential under As flux [25]. In its high-temperature regime, where the surface is mostly covered by the $c(8 \times 2)$ phase, the

*PereiroViterboJ@cardiff.ac.uk

(6×6) enters a state of metastability, with patches appearing and disappearing dynamically [26]. In between the two regimes lies a broad $(6 \times 6) \leftrightarrow c(8 \times 2)$ transition, where a stable coexistence between the two phases is observed under a large spectrum of temperatures during the transition [27,28]. These observations contradict surface energy calculations, which exclude the (6×6) from the sequence of phase transitions altogether. It was suggested that since calculations are done at $T = 0$ K, the entropy difference at nonzero temperatures could be responsible for the stabilization of the otherwise unfavorable (6×6) phase [25].

We show that with the unified method, we are able to fill this gap between theory and experiment, as we explore the (6×6) phase and gain valuable insights from its coexistence with the $c(8 \times 2)$.

II. EXPERIMENTAL PROCEDURE

Details on the experimental setup and initial surface preparation are given in the Appendix 2.

First, experiments are done to determine the behavior of the coverage against varying temperature. The measurements are done by changing the temperature in small steps between 500 °C and 620 °C and monitoring the phase transition between the $c(8 \times 2)$ and the (6×6) phases. Figure 1 shows the variation in coverage for the full range of temperatures and the corresponding images at chosen temperatures during the experiment. At higher temperatures, up to 620 °C, the $c(8 \times 2)$ dominates the surface, with the (6×6) becoming unstable above 580 °C, entering a state of metastability [26]. At 550 °C, the coverage of $c(8 \times 2)$ and (6×6) equalizes, and at lower temperatures, between 550 °C and 500 °C, the (6×6) covers the majority of the surface. The patterns are proven to be thermodynamically stable, retaining a constant coverage during observations for a period of 3–4 h. The reversibility of the process is verified by repeating the same procedure for both heating and cooling down the surface, where some hysteresis was observed. The observations indicate that the transition between the (6×6) and the $c(8 \times 2)$ phases is first order, as the contrasting areas in the images show that the boundaries between the (6×6) and $c(8 \times 2)$ patches are sharp.

Then, fluctuation monitoring experiments are done with the temperature set to 550 °C, where the coexistence between the (6×6) and $c(8 \times 2)$ phases is at about equal coverage. The surface is allowed to stabilize and selected suitable regions are imaged for 3–6 min each. With these conditions, imaging was done with frame rates of between and 20 fps with sufficient signal-to-noise ratio and a lateral resolution of about 10 nm. Fluctuations detection and processing was designed in such a way as to accommodate different boundary sizes and shapes, and to work well in a variety of imaging conditions. This extends the application of the method to materials that do not necessarily exhibit a particular structural order in their steps and boundaries, just like the GaAs(001) surface examined in this work. The algorithm's process of detecting boundaries is shown in Fig. 2 and the process of converting the boundaries to fluctuations data is visualized in Fig. 3. The algorithm's final output is the distance offset of each detection with respect to the average position over the
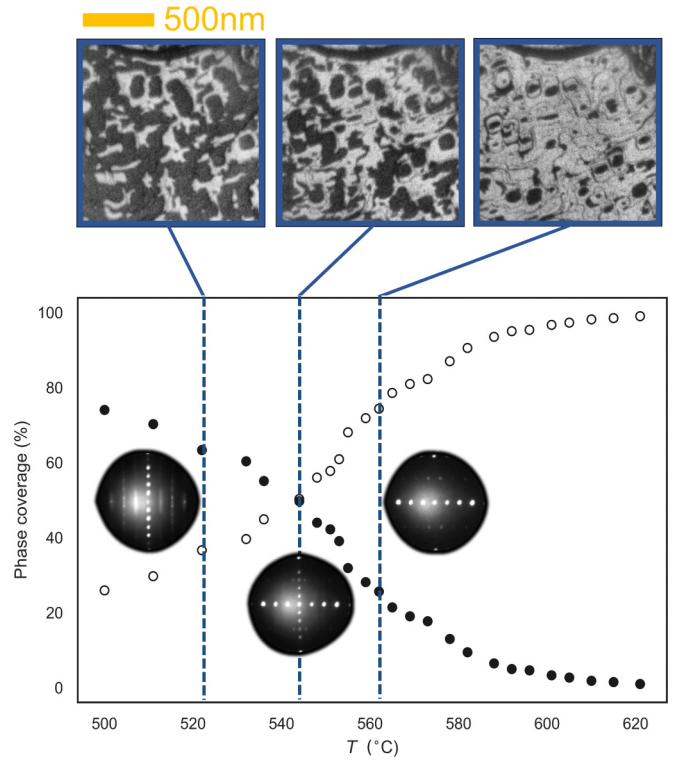

FIG. 1. A diagram of the full coverage variation between the $c(8 \times 2)$ (white dots) and (6×6) (black dots) phases with temperature. LEEM images of the dark (6×6) domains and the bright $c(8 \times 2)$ domains are shown at the corresponding temperatures. The images show how the coverage of the (6×6) decreases as the temperature is increased. Low-energy electron diffraction images show the diffraction patterns at the temperature regions with different coverage proportions of the two phases. The diffraction pattern in the middle of the range, at around equal coverage, is a mixture of the (6×6) and the $c(8 \times 2)$ patterns in the low- and high-temperature range, respectively.

whole experiment, as detected in every image of the video by the initially constructed frame of reference.

III. RESULTS

In order to explore the coexistence during the transition, we perform analysis over two complementary steps: analysis of the phase coverage and analysis of the phase boundaries [3].

A. Phase coverage

Phase coexistence occurs when the energy gain from creating and subsequently maintaining an unfavorable phase and its boundaries is compensated by the elastic and electrostatic interactions at those phase boundaries, which allow local relaxation. The total surface energy per unit area is [19]

$$
\begin{aligned}
E_{\text{total}} = {} & \frac{C_0}{L_t} + p\frac{\Delta S(T - T_0)}{2} - \frac{2C_m}{L_t}\ln\left(\frac{L_t}{\pi a}\cos\left(\frac{p\pi}{2}\right)\right) \\
& + \frac{C_d}{L_t^2}\tan\left(\frac{p\pi}{2}\right) - \frac{8C_r}{L_t^3}\left(\frac{1}{(1+p)^2} + \frac{1}{(1-p)^2}\right).
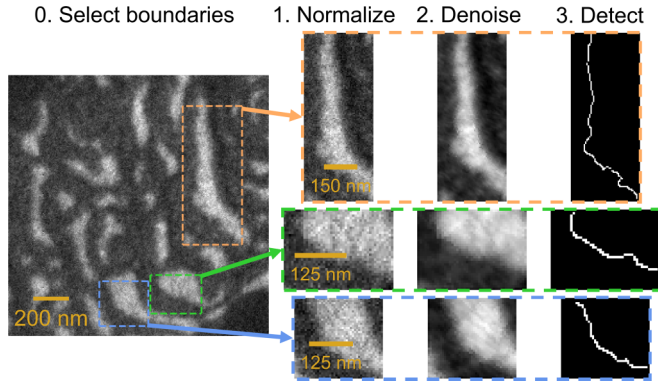\end{aligned}
$$

(1)

FIG. 2. The process of extracting boundary coordinates from raw images through edge detection. Boundaries are marked by the user and isolated (step 0). After that, the following methods, corresponding to the illustrated steps, are applied to each video frame: 1. Normalization: The selections are normalized linearly or through contrast-limited adaptive histogram equalization [29], depending on intensity gradients and noise levels in the image section. 2. Bilateral Denoising: A nonlinear edge-preserving denoising method is applied to filter noise without destroying small features [30,31]. 3. Canny-Devernay Detection: A subpixel variant of the powerful and stable Canny edge detection is applied, giving the boundary positions for each video frame with subpixel accuracy [32,33]. The size of each pixel is equivalent to 6 nm. In total, about 15 500 video frames were analyzed, producing sets of coordinates for ten boundaries.

Here, $p = (2\frac{A_{(6\times6)}}{A_{\text{total}}} - 1)$ is the surface coverage parameter. It is defined with the areas of (6×6) and $c(8 \times 2)$ coverage, such that it expresses the asymmetry between the two phases. It varies from $p = -1$ for full $c(8 \times 2)$ coverage to $p = 1$ for full (6×6) coverage. $T_0 \approx 550\,°\text{C}$ is the temperature where the two phases have equal coverage, ΔS is the difference in entropy between the phases, and L_t is the distance between steps, or terrace width. This expression can then be minimized with respect to the coverage, $\partial E / \partial p = 0$, to give a dependence between coverage and temperature.

$$T - T_0 = -\left(\frac{2}{\Delta S}\right)\left[\frac{\pi C_m}{L_t}\tan\left(\frac{p\pi}{2}\right) + \frac{\pi C_d}{2L_t^2}\cos^{-2}\left(\frac{p\pi}{2}\right)\right.$$
$$\left. + \frac{16Cr}{L_t^3}\left(\frac{1}{(1+p)^3} - \frac{1}{(1-p)^3}\right)\right] + \text{const.} \quad (2)$$

A fitting of the experimental data is shown in Fig. 4 and yields the constants in Eq. (1). The C_0 term accounting for the boundary creation energy costs vanishes with the differentiation. From the fit, the value of the constant representing the elastic and electrostatic interactions at the phase boundaries is $C_m = 6.4$ meV Å^{-1}, the interaction between boundaries and steps, $C_d = 8.65$ eV, the short-range boundary-boundary interactions, $C_r = 57.8$ eVÅ, and the difference in entropy is $\Delta S = 7.2 \times 10^{-4}$ meV K^{-1} Å^{-2}. To estimate the values of the C_d and C_r parameters more accurately, the fitted values of C_m and ΔS are bound to within an order of magnitude of the values derived in the fluctuations analysis.

The higher-order interaction terms C_d and C_r have a negligible contribution at the regions of equal coverage $p \approx 0$ [19],
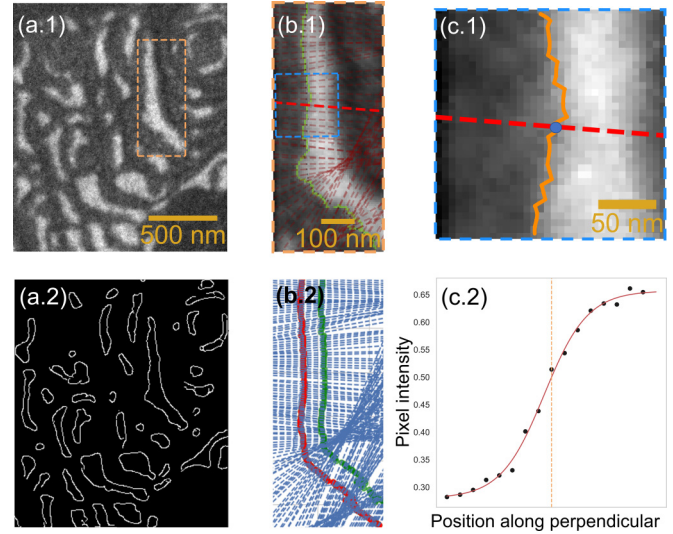

FIG. 3. The logical steps of the algorithm for converting the detected boundary coordinates to fluctuations (offsets). (a.1) shows the area of the selected boundary for which the boundary coordinates were gathered and (a.2) gives an example of the edge detection for the whole area. The precise detection for each frame is shown in Fig. 2. The detected boundary from the first frame of the LEEM video is used to construct perpendiculars which adapt to the boundary's general shape, allowing for boundaries of arbitrary shapes to be analyzed without additional bias (b.1). The constructed perpendiculars, shown in full in (b.2), are the reference frame to which all detected points are aligned. The detection points from the Canny-Devernay algorithm are projected onto the reference frame by finding the crossing points with the perpendiculars using WENO interpolation [34]. (c.1) shows how the detected boundary around an example perpendicular from the reference frame is interpolated and crossed with the perpendicular to produce a data point. The image intensity profile along that perpendicular is shown in (c.2) at the example detected point position, demonstrating the positional accuracy of the detection. In total, over 3.1 million data points were analyzed with this method.

giving a linear dependence:

$$\tan\left(\frac{p\pi}{2}\right) \approx -\frac{L_t \Delta S}{2\pi C_m}(T - T_0). \quad (3)$$

As can be seen in the linear fit shown in Fig. 4, experimental data agrees with the linear behavior indicated by Eq. (3) around equal coverage. This is a strong indication that the elastic relaxation at the boundaries is the most important interaction that contributes towards the observed coexistence [3]. The linear fit yields a relation between the entropy difference ΔS and C_m, which can be used to calculate the entropy difference [19]. Given the terrace sizes on the GaAs(001) surface where the measurements made during the experiment are $L_t = (185 \pm 13)$ nm, the slope corresponds to

$$\frac{\Delta S}{C_m} = (1.06 \pm 0.20) \times 10^{-4} \text{ K}^{-1} \text{ Å}^{-1}. \quad (4)$$

B. Boundary fluctuations

The value of C_m can be obtained by analyzing the boundary fluctuations between the two phases in the coexistence. In
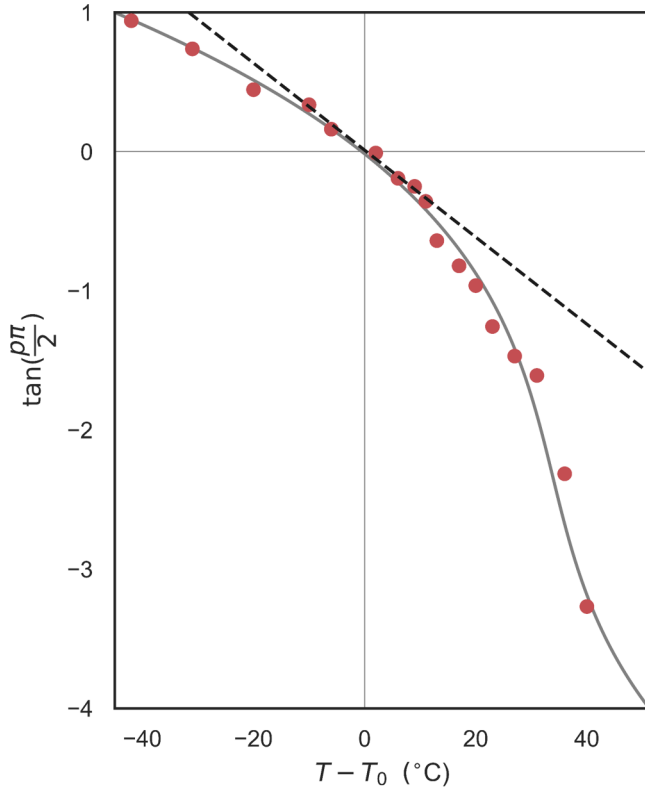
FIG. 4. Experimental results (red dots) of dependence of $\tan(\frac{p\pi}{2})$ on the temperature T. The gray curve is a fit from the minimization of Eq. (1) and the dashed linear fit represents the linear dependence expected at around equal coverage [Eq. (4)]. The slope of the fit is (-0.031 ± 0.002) K^{-1} and gives us the result in Eq. (4).

Eq. (4), C_m is the sum of the contributions from electrostatic interactions,

$$C_\phi = \frac{(\Delta\phi)^2}{8\pi^2} \quad (5)$$

coming from the work function difference $\Delta\phi$ between the two phases, and elastic interactions,

$$C_\lambda = (\Delta\lambda)^2 \frac{(1-\nu^2)}{\pi\Upsilon}, \quad (6)$$

arising from the stress difference $\Delta\lambda$ between the two phases, where $\nu = 0.31$ is Poisson's ratio and $\Upsilon = 0.53$ eV/Å^3 is Young's modulus [16,19]. The difference in work functions between the two phases can be found experimentally by using the transition between mirror mode and LEEM mode in the microscope imaging of each phase [35], giving $\Delta\phi = 0.1$ eV. This results in an electrostatic interaction constant of $C_\phi = 0.01$ meV Å^{-1}.

The stress difference $\Delta\lambda$ is found through measurements of the phase boundary fluctuations [36,37] at the temperature of equal coverage $T_0 = 550$ °C. The phase boundary fluctuations are closely imaged at 15 fps for about 4 min and processed as shown in Figs. 2 and 3. These imaging conditions push the LEEM to the limits of its temporal and spatial resolution capabilities.

The boundary fluctuations are defined as the offsets $y(x, t)$ of each point x along the boundary for a unit time t. In prac-
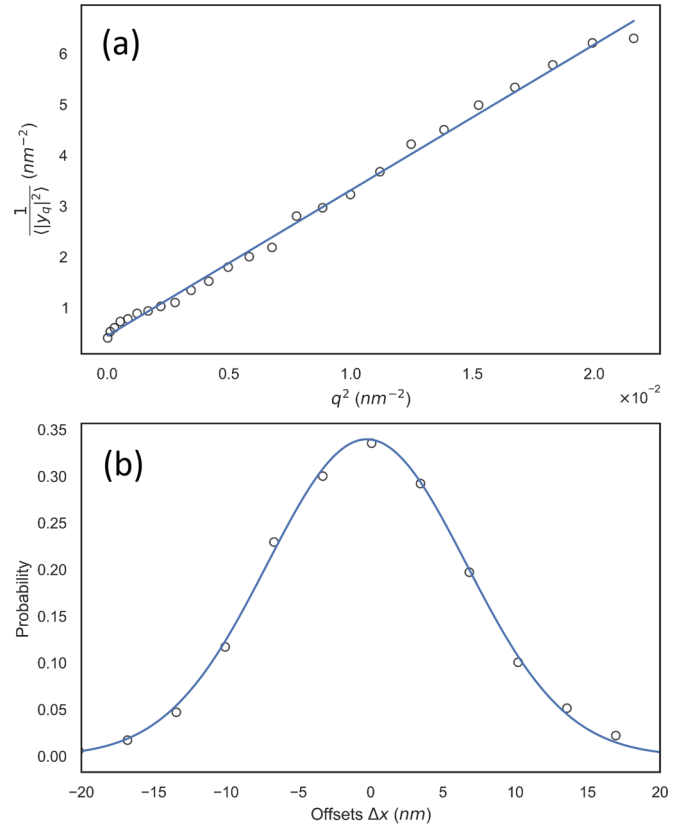

FIG. 5. Example of the fluctuations analysis. These results were generated for the marked edge in Fig. 3. (a) A linear fit of the Fourier components of the boundary fluctuations [Eq. (8)]. The slope of the fit is $\frac{L_b\beta}{k_BT}$. (b) Probability distribution of the boundary fluctuations [Eq. (9)]. The measured standard deviation over all the data is $\sigma = (5.88 \pm 1.08)$ nm.

tice, that is the measured point offset for each image frame, with respect to its average position over all frames. These measurements are first used to find the boundary stiffness β. Through the Fourier transformation in the form

$$y_q(t) = \frac{1}{N} \sum_q y(x, t) \exp(-iqx), \quad (7)$$

the Fourier components can be analyzed. The mean squared Fourier components of the deflections $\langle|y_q^2|\rangle$ can be expressed as [37]

$$\langle|y_q^2|\rangle = \frac{k_BT}{L_b\beta q^2}, \quad (8)$$

where k_B is the Boltzmann constant, L_b is the length of the explored boundary, and $q = 2\pi n/L_b$, where $n = 1, 2, \ldots, N$. This gives a linear relationship between $\langle|y_q^2|\rangle^{-1}$ and q^2. The linear fit to the data, using Eq. (8) as shown in Fig. 5(a), gives a boundary stiffness of $\beta = (28.3 \pm 11.0)$ meV nm^{-1}. The linearity of the experimental data, when adapted for Eq. (8), is an indication of how independent the fluctuations of each analyzed boundary are.

The boundary stiffness is used to find C_λ using the probability distribution of the phase boundary deflections, shown in Fig. 5(b). The standard deviation of the Gaussian fit to the

data corresponds to the expected distribution, given by [37]:

$$\sigma^2 = \frac{k_B T L_t}{2\pi (2\beta C_\lambda)^{1/2}}. \tag{9}$$

From Eq. (9), the value of the elastic contributions constant is $C_\lambda = (9.75 \pm 6.06)$ meV Å^{-1}. Using Eq. (6), we are then able to find the stress difference $\Delta\lambda = (0.15 \pm 0.05)$ eV Å^{-2}.

The much larger value of C_λ compared to C_ϕ suggests the elastic contributions are prevalent during the coexistence. We can now find $C_m = (9.76 \pm 6.06)$ meV Å^{-1}, and so, from Eq. (4), we can obtain the value for the entropy difference $\Delta S = (10.32 \pm 6.82) \times 10^{-4}$ meV K^{-1} Å^{-2}.

IV. CONCLUSION

The uncertainties in the results are in part due to the disordered nature of the surface steps configurations, affecting interactions at each individual boundary and giving a spread in the measured values for every analyzed boundary. Nonetheless, the behavior of the coverage, as seen in Fig. 4, fits the predicted behavior, providing a relationship between the entropy and elastic interactions at the boundaries that enables us to reach fundamental conclusions on the thermodynamics of the system. Despite the chaotic nature of the step arrangements and the complexity of the compound material, the coexistence in GaAs(001) obeys the same rules as the coexistence in a more predictable and thoroughly detailed system, such as the one in Si(111) between the (1×1) and (7×7) phases [19], giving confidence in the broad applicability of the method. The density-functional theory (DFT) calculations in previous works show that none of the available (6×6) models are stable at $T = 0$ K [11]. By contrast, experiments are conducted at a range of temperatures around $T_0 \approx 550\,^\circ$C, which has led to the suggestion that the entropy difference due to configurational entropy can help stabilize the (6×6) with its contribution to the formation energy [23,25]. In the context of the (6×6), the entropy difference found above contributes to the formation energy with

$$T_0 \Delta S = (13.6 \pm 9.0) \text{ meV } [(1 \times 1) \text{ cell}]^{-1}. \tag{10}$$

The contribution to the formation energy needed to stabilize the most energetically favorable (6×6) structure models is approximately 50 meV $[(1 \times 1)$ cell$]^{-1}$ [25]. The contribution from the entropy difference in Eq. (10) is not negligible, but not large enough to stabilize the (6×6) with respect to the $c(8 \times 2)$ by itself. These results strongly suggest that the (6×6) phase is not stable and the elastic relaxation associated to the phase boundaries is necessary to stabilize it.

In conclusion, we propose a methodology that brings together separate experimental methods that are well established within the LEEM community to provide an estimate of the entropy change between surface phases. The unified technique demonstrates the ability of LEEM microscopy to provide insight on elusive, but key thermodynamical parameters in semiconductors through a unitary, self-contained method. We show the applicability of the method on complex semiconductor materials and develop computational methods that generalize the approach to surfaces with irregular step geometry. With that, the developed method is capable of giving straightforward access to the entropy difference and stress

difference between two coexisting phases on many semiconductor surfaces, adding valuable insights on phase transitions that can have a significant impact on surface science. Using the unified method, we resolve an important uncertainty around the surface energetics of GaAs(001), namely, we show that for the temperature spectrum where the (6×6) is observed in its coexistence regime, it is still the unfavorable phase, but the elastic relaxation at the boundaries during its coexistence with the $c(8 \times 2)$ phase is a key contribution to reach the lowest energy state of the surface and enable its stability.

APPENDIX

1. Background on density functional theory calculations

DFT is the main tool for theoretically describing the energetics of a surface reconstruction. In GaAs(001), it is used to derive the zero-temperature formation free energies of different structures and to plot them against the gallium chemical potential μ_{Ga} to get a phase diagram for its surface. With this approach, many models for the (6×6) have been proposed, such as Kuball [39], McLean [40], Xu [41], and Kocan [42], but all of them suggest a high formation energy, making them inaccessible on a real GaAs(001) surface. The likeliest candidate out of all them is the Kocan model, as it possesses the lowest free energy. To make that model more accessible, modifications were also proposed, adjusting the proportions of As-As dimers, resulting in the most likely candidate for the (6×6) structure so far—a (12×6)-sized unit cell [23]. However, this optimal structure is still not stable at any chemical potential value, suggesting a $\beta 2(2 \times 4) \rightarrow c(8 \times 2)$ phase transition sequence. By contrast, experiments show a $\beta 2(2 \times 4) \rightarrow (3 \times 6) \rightarrow (6 \times 6) \rightarrow c(8 \times 2)$ transition.

2. Experimental setup

Experiments were performed using the Elmitec LEEM-III microscope. Using very low energy electrons (0–15 eV) makes the LEEM highly sensitive to the structure of the crystal surface, allowing real-time nonscanning *in situ* observation of the processes occurring on a crystal surface under a variety of conditions, with high lateral resolution [43]. A GaAs(001)

sample is placed under ultrahigh vacuum of around 2×10^{-10} Torr; its surface is initially prepared by annealing for 2 h at 580 °C. Gallium droplets of up to 5 μm in diameter are then produced at 620 °C and allowed to run on the surface, creating flat regions of at least 15 μm length [44,45]. After the atomically flat surface is created, the droplets are slowly evaporated at temperatures of around 530 °C. The sample is then brought up to 550 °C, which is in the middle of the temperature region where both the $c\,(8 \times 2)$ and the (6×6) phases can be found [27]. The forming domains are always monitored and maintained for enough time to ensure equilibrium before an experiment is conducted. The phases are confirmed by observing the low-energy electron diffraction patterns at select small surface patches (μLEED) and the discrimination of phases can be further enhanced by utilizing the high contrast between phases using dark field with a selected electron energy, optimized for each phase (SEDFLEEM), as described in [28], with the consequence of a lower overall image intensity.

The coverage experiments were done in dark field, by switching between the (1/4, 0) spot with an electron beam energy of 6.2 eV to observe the $c\,(8 \times 2)$, and the (3/6, 0) spot of the (6×6) at an energy of 7.8 eV. The fluctuation experiments were all done in bright field at 8.5 eV electron beam energy.

3. Work function difference measurement

The work function difference between the (6×6) and $c\,(8 \times 2)$ phases was measured by varying the start voltage from -1.5 to 2.5 eV. The energies, corresponding to the largest intensity variation, are found for both phases, the difference of which gives the work function difference in eV. It is found that the work function difference has an insignificantly small contribution to the results, compared to contributions from elastic interactions.

4. Computational algorithms

Here, we give a short summary of the procedures in each of the developed algorithms. Algorithm 1 takes raw images that go through a preprocessing procedure and detects the selected boundary in each image sequentially, outputting a list of boundary coordinates. Algorithm 2 takes the output of Algorithm 1 and transforms it into boundary offsets, outputting data that represents the boundary fluctuations in a robust and unbiased manner. Algorithm 3 takes the boundary offsets data and analyzes it, as described in Sec. III, outputting and recording the sought parameters and generating relevant graphical representations of the analysis. The importing of raw images in Python is done through the convenience of Lin Zhu's package [46] and the images are processed using the SCIKIT-IMAGE Python package [47].

Algorithm 1. Detecting a phase boundary.

Input: Ordered list of Raw Images
Output: Coordinates of each point on selected edge at each frame
1: **for** *first image* **do** Save template in-memory for `Alignment`   ▷ If images drifting with time
2:     Get user-generated *mask* of selected edge
3: **for each** *image* ∈ all frames **do** `Alignment` to saved template
4:     Cut image to fit mask
5:     `Normalization through Histogram Equalization`
6:     `Bilateral Denoising`
7:     `Canny-Devernay Edge Detection` **with** applied mask
8:     Collect detected edge coordinates
9: Save coordinates to disk; *shape:* [frame, [x-coords, y-coords]]

Algorithm 2. Extracting boundary fluctuations.

Input: Detected Edge Coordinates
Output: Edge fluctuation w.r.t. mean position
1: Load coordinates of detected edge for each frame from Algorithm 1
2: **for** *edge coordinates* of first frame **do**
3:     **for each** point on edge **do**
4:         Get neighboring N points
5:         Smooth by approximating with `Ramer Douglas Peucker algorithm`
6:         Fit straight line segment through approximated polygon
7:         Build line segment *bisector*
8:     Save all *bisectors*
9: **for each** *edge coordinates* ∈ rest of frames **do**
10:     **for all** *bisectors* **do**
11:         Find closest N points out of all points on edge
12:         Do `WENO interpolation` between points
13:         Cross interpolation with *bisector* and save position
14: **for each** *bisector* **do**
15:     Find mean position of all points on bisector
16:     Subtract mean from all points' positions
17: Save all positions: shape: [position on each bisector, frame]

Algorithm 3. Analyzing boundary fluctuations.

Input: Boundary fluctuations for one edge
Output: Distribution analysis and FFT analysis
1: **procedure** FOURIER TRANSFORM
2:     Load data of boundary fluctuations from Algorithm 2
3:     **for all** frames **do**
4:         `Fast Fourier Transform` of boundary offsets at each frame to find y_q^2 in Eq. (7) in the Main Text
5:     Perform linear fit of $\frac{1}{y_q^2}$ against q^2 and get slope
6:     **return** resulting β from slope of fit
7: **procedure** FLUCTUATIONS DISTRIBUTION
8:     Load data of boundary fluctuations from Algorithm 2
9:     `Compute histogram` of data ▷ Only spatial distribution matters here
10:     Fit Gaussian to histogram, as predicted by Eq. (9)
11:     **return** mean, standard deviation of Gaussian

---

[1] W. Telieps and E. Bauer, The $(7 \times 7) \leftrightarrow (1 \times 1)$ phase transition on Si(111), Surf. Sci. **162**, 163 (1985).

[2] W. Telieps and E. Bauer, Kinetics of the $(7 \times 7) \leftrightarrow (1 \times 1)$ transition on Si(111), Berich Bunsen Gesell. Phys. Chem. **90**, 197 (1986).

[3] J. B. Hannon and R. M. Tromp, Low-energy electron microscopy of surface phase transitions, Annu. Rev. Mater. Res. **33**, 263 (2003).

[4] H. Ibach, The role of surface stress in reconstruction, epitaxial growth and stabilization of mesoscopic structures, Surf. Sci. Rep. **29**, 195 (1997).

[5] B. A. Joyce and D. D. Vvedensky, Self-organized growth on GaAs surfaces, Mater. Sci. Eng. R **46**, 127 (2004).

[6] T. J. Krzyzewski and T. S. Jones, Nanostructure formation in InAs/InP(001) heteroepitaxy: Importance of surface reconstruction, Phys. Rev. B **78**, 155307 (2008).

[7] T. Yasuda, N. Miyata, and A. Ohtake, Influence of initial surface reconstruction on the interface structure of HfO$_2$/GaAs, Appl. Surf. Sci. **254**, 7565 (2008).

[8] A. Ohtake, A. Hagiwara, and J. Nakamura, Controlled incorporation of Mn in GaAs: Role of surface reconstructions, Phys. Rev. B **87**, 165301 (2013).

[9] A. Ohtake, T. Mano, A. Hagiwara, and J. Nakamura, Self-assembled growth of Ga droplets on GaAs(001): Role of surface reconstructions, Cryst. Growth Des. **14**, 3110 (2014).

[10] J. W. Orton and C. T. Foxon, *Molecular Beam Epitaxy: A Short History* (Oxford University Press, Oxford, 2015).

[11] M. Pristovsek, S. Tsukamoto, A. Ohtake, N. Koguchi, B. G. Orr, W. G. Schmidt, and J. Bernholc, Gallium-rich reconstructions on GaAs(001), Phys. Status Solidi B **240**, 91 (2003).

[12] V. P. LaBella, M. R. Krause, Z. Ding, and P. M. Thibado, Arsenic-rich GaAs(001) surface structure, Surf. Sci. Rep. **60**, 1 (2005).

[13] A. Ohtake, Surface reconstructions on GaAs(001), Surf. Sci. Rep. **63**, 295 (2008).

[14] O. L. Alerhand, D. Vanderbilt, R. D. Meade, and J. D. Joannopoulos, Spontaneous Formation of Stress Domains on Crystal Surfaces, Phys. Rev. Lett. **61**, 1973 (1988).

[15] D. Vanderbilt, Elastic stress domains on the Si(100) surface, J. Vacuum Sci. Technol., B: Microelectron. Nanometer Struct.–Process., Meas., Phenom. **7**, 1013 (1989).

[16] D. Vanderbilt, Phase segregation and work-function variations on metal surfaces: Spontaneous formation of periodic domain structures, Surf. Sci. **268**, L300 (1992).

[17] K. O. Ng and D. Vanderbilt, Stability of periodic domain structures in a two-dimensional dipolar model, Phys. Rev. B **52**, 2177 (1995).

[18] P. Müller and A. Saúl, Elastic effects on surface physics, Surf. Sci. Rep. **54**, 157 (2004).

[19] J. B. Hannon, F.-J. Meyer zu Heringdorf, J. Tersoff, and R. M. Tromp, Phase Coexistence during Surface Phase Transitions, Phys. Rev. Lett. **86**, 4871 (2001).

[20] C. Alfonso, J. Bermond, J. Heyraud, and J. Métois, The meandering of steps and the terrace width distribution on clean Si(111), Surf. Sci. **262**, 371 (1992).

[21] N. C. Bartelt, J. L. Goldberg, T. L. Einstein, and E. D. Williams, The equilibration of terrace width distributions on stepped surfaces, Surf. Sci. **273**, 252 (1992).

[22] https://github.com/M-A-Ivanov/LEEM_SubPixelEdgeAnalysis.

[23] K. Seino, W. G. Schmidt, and A. Ohtake, Ga-rich GaAs(001) surface from *ab initio* calculations: Atomic structure of the (4×6) and (6×6) reconstructions, Phys. Rev. B **73**, 035317 (2006).

[24] A. Ohtake, Structure and composition of Ga-rich (6×6) reconstructions on GaAs(001), Phys. Rev. B **75**, 153302 (2007).

[25] C. X. Zheng, K. Hannikainen, Y. R. Niu, J. Tersoff, D. Gomez, J. Pereiro, and D. E. Jesson, Mapping the surface phase diagram of GaAs(001) using droplet epitaxy, Phys. Rev. Materials **3**, 124603 (2019).

[26] K. Hannikainen, D. Gomez, J. Pereiro, Y. R. Niu, and D. E. Jesson, Surface Phase Metastability during Langmuir Evaporation, Phys. Rev. Lett. **123**, 186102 (2019).

[27] C. X. Zheng, J. Tersoff, W. X. Tang, A. Morreau, and D. E. Jesson, Novel GaAs surface phases via direct control of chemical potential, Phys. Rev. B **93**, 195314 (2016).

[28] Y. R. Niu, J. Pereiro, D. Gomez, and D. E. Jesson, Selected energy dark-field imaging using low energy electrons for optimal surface phase discrimination, Ultramicroscopy **200**, 79 (2019).

[29] S. M. Pizer, E. P. Amburn, J. D. Austin, R. Cromartie, A. Geselowitz, T. Greer, B. ter Haar Romeny, J. B. Zimmerman, and K. Zuiderveld, Adaptive histogram equalization and its variations., Comput. Vision Graph., Image Process. **39**, 355 (1987).

[30] P. Jain and V. Tyagi, A survey of edge-preserving image denoising methods, Inf. Syst. Frontiers **18**, 159 (2016).

[31] C. Tomasi and R. Manduchi, Bilateral filtering for gray and color images, *Sixth International Conference on Computer Vision, Bombay, India* (IEEE Cat. No. 98CH36271, 1998), pp. 839–846, doi: 10.1109/ICCV.1998.710815.

[32] J. Canny, A computational approach to edge detection, IEEE Trans. Pattern Anal. Mach. Intell. **PAMI-8**, 679 (1986).

[33] F. Devernay, A non-maxima suppression method for edge detection with sub-pixel accuracy, INRIA Research Report No. 2724 (1995), https://hal.inria.fr/inria-00073970.

[34] G. Janett, O. Steiner, E. Alsina Ballester, L. Belluzzi, and S. Mishra, A novel fourth-order WENO interpolation technique, Astron. Astrophys. **624**, A104 (2019).

[35] C. M. Yim, K. L. Man, X. Xiao, and M. S. Altman, Low-energy electron microscopy of CO/Pt(111) surface diffusion by nonequilibrium coverage profile evolution, Phys. Rev. B **78**, 155439 (2008).

[36] N. C. Bartelt, W. Theis, and R. M. Tromp, Ostwald ripening of two-dimensional islands on Si(001), Phys. Rev. B **54**, 11741 (1996).

[37] J. B. Hannon and R. M. Tromp, Phase boundary fluctuations on Si(111), J. Vac. Sci. Technol., A **19**, 2596 (2001).

[38] http://doi.org/10.17035/d.2022.0216365941.

[39] M. Kuball, D. T. Wang, N. Esser, M. Cardona, J. Zegenhagen, and B. O. Fimland, Microscopic structure of the GaAs(001)-(6×6) surface derived from scanning tunneling microscopy, Phys. Rev. B **51**, 13880 (1995).

[40] J. G. McLean, P. Kruse, and A. C. Kummel, Atomic structure determination for GaAs(001)-(6×6) by STM, Surf. Sci. **424**, 206 (1999).

[41] H. Xu, Y. G. Li, A. T. Wee, C. H. Huan, and E. S. Tok, On STM imaging of GaAs(001)-$(n \times 6)$ surface reconstructions: Does the (6×6) structure exist, Surf. Sci. **513**, 249 (2002).

[42] P. Kocán, A. Ohtake, and N. Koguchi, Structural features of Ga-rich GaAs(001) surfaces: Scanning tunneling microscopy study, Phys. Rev. B **70**, 201303 (2004).

[43] E. Bauer, *Surface Microscopy with Low Energy Electrons* (Springer-Verlag, New York, 2014).

[44] J. Tersoff, D. E. Jesson, and W. X. Tang, Running droplets of gallium from evaporation of gallium Aarsenide, Science **324**, 236 (2009).

[45] C. Zheng, W.-X. Tang, and D. E. Jesson, Planar regions of GaAs(001) prepared by Ga droplet motion, J. Vac. Scie. Technol., A **34**, 043201 (2016).

[46] https://github.com/zhulincqu/LEEMimage.

[47] S. van der Walt, J. L. Schönberger, J. Nunez-Iglesias, F. Boulogne, J. D. Warner, N. Yager, E. Gouillart, and T. Yu, scikit-image: image processing in Python, PeerJ **2**, e453 (2014).